Applied Surface Science 473 (2019) 564–570

Contents lists available at ScienceDirect

Applied Surface Science

journal homepage: www.elsevier.com/locate/apsusc

Full Length Article

# Pressure induced semiconductor-metallic transition of selenium nanoribbons generated by laser ablation in liquids

Yunyu Cai[a,*], Yixing Ye[a], Pengfei Li[a], Yonghui Zhou[b], Jun Liu[a], Zhenfei Tian[a], Zhaorong Yang[b], Changhao Liang[a,*]

[a] Key Laboratory of Materials Physics and Anhui Key Laboratory of Nanomaterials and Nanotechnology, Institute of Solid State Physics, Hefei Institutes of Physical Science, Chinese Academy of Sciences, Hefei 230031, Anhui, China

[b] Anhui Province Key Laboratory of Condensed Matter Physics at Extreme Conditions, High Magnetic Field Laboratory, Chinese Academy of Sciences, Hefei 230031, Anhui, China

ARTICLE INFO

*Keywords:*
Selenium nanoribbons
Semiconductor-metallic transition
High pressure
Phase transition
Laser ablation

ABSTRACT

Single crystalline Selenium (Se) nanoribbons with large length-diameter ratio was catalytically synthesized by laser ablation in liquids. In this study, the unique growth, pressure-dependent phase evolution and superconducting transition of Se nanoribbons are systematically investigated. Importantly, we first found that the semiconductor-metal transition pressure of such Se nanoribbons located at 11.1 GPa at room temperature, which was extremely close to the theoretically predicated value of 11.16 GPa of hexagonal Se. The structure evolution of Se nanoribbons revealed via in situ Raman spectrum indicated three subsequent phase transition stages. The temperature dependence of resistance measurements revealed the occurrence of superconducting state of monoclinic Se at 11.8 GPa, which is markedly lower than reported pressures to date. The phase transition barrier attenuation originating from the volumetric contraction of Se lattice is assumed to offset the influences of temperature and surface energy in low-dimensional Se nanoribbons with large length-diameter ratios, resulting in a transition pressure approaching the predicted value.

## 1. Introduction

As a single elemental semiconductor, selenium (Se) has attracted tremendous attention owing to its unique properties, such as large piezoelectric and thermoelectric effects, high photoconductivity, and nonlinear optical responses [1,2]. Importantly, Se can undergo superconducting transition under high pressure [3,4]. For hexagonal Se (Se-I) as the most stable state at ambient pressure, upon compression, it can successively undergo an intermediate phase (Se-II), monoclinic structure (Se-III), orthorhombic structure (Se-IV), β-Po type (Se-V), and bcc phase (Se-VI) at room temperature [5]. Semiconductor to metallic (S-M) transition has been thought as the indication of a superconductor phase for selenium [6]. Many literatures proved that S-M transition of hexagonal Se occurs between 13–23 GPa at room temperature accompanied with the emergence of monoclinic phase which is cryogenic superconductive [5–8]. Noting that, the theoretical calculation proposed that dropping temperature could decrease the energy barrier in transition so that the S-M transition point of hexagonal Se is approximately 11.16 GPa at absolute zero (0 K) [9]. Although many tests have been conducted on various Se polymorphs [10,11], the difference in transition pressure point between the predicted and experimental values remain because it is impossible to really conduct experiments at absolute zero.

Interestingly, to substitute nanocrystal materials for the bulk has been the upspringing strategy for studying pressure induced phase transition processes due to the size and/or morphology effect [12,13]. According to Eqs. (1) and (2), the energy barrier involved in phase transition is dependent on surface energy change and volumetric contraction [13]. Larger surface energy change can lead to a higher energy barrier indicating a higher transition pressure, whereas larger volumetric contraction works adversely. That's why some nanocrystallines exhibit different transition processes [12,14–18], e.g. higher or lower phase transition pressures than those of the corresponding bulk materials.

For one dimensional (1-D) nanocrystals with large length-diameter ratios, the excellent compressibility of lattice in the growth direction under pressure tends to decrease the energy barrier largely [12,19]. However, for many years, the direct observation of S-M transition of Se nanostructures is still limited. Liu et al. just have revealed that the difference of transition sequence between Se nanocrystalline

* Corresponding authors.
*E-mail addresses:* yycai@issp.ac.cn (Y. Cai), chliang@issp.ac.cn (C. Liang).

https://doi.org/10.1016/j.apsusc.2018.12.183
Received 27 August 2018; Received in revised form 17 November 2018; Accepted 19 December 2018
Available online 20 December 2018
0169-4332/ 

(Φ ~ 13 nm) and the bulk Se [20]. Although Ding et al. have observed the hexagonal to monoclinic transition of Se nanowires at 18.1 GPa [21], the transition pressure was still higher than the theoretical value.

Here, we designed single crystal Se nanoribbons with a large length-diameter ratio which is of excellent compressibility. Such single crystal nanoribbons are spontaneously grown from Se nanoparticles in colloid solution with the catalytic assistance of Sb nanoparticles. Both of Se nanoparticles and Sb nanoparticles were generated by laser ablation of Se and Sb solid targets in pure water successively. The structure evolution of Se nanoribbons was analyzed via in situ Raman spectrum from atmospheric pressure to 44.8 GPa at room temperature. At 11.1 GPa, the monoclinic Se phase appeared, and the S-M transition was demonstrated by the corresponding resistance measurement. Surprisingly, these results were precisely close to the theoretically predicted value. The influence of surface energy and volumetric change in Se nanoribbons were further discussed. To the best of our knowledge, no study has reported S-M transitions, in good agreement with theoretical predictions, of hexagonal Se nanoribbons at extremely low pressures.

## 2. Experimental and theoretical methods

### 2.1. Gibbs free energy difference deduction

The energy barrier calculations were based on the total Gibbs free energy difference between hexagonal and monoclinic of Se polymorphs in combination with the surface energy contribution [13]. Eq. (1) shows Gibbs energy of nanostructure:

$$G = U - TS + PV + \sigma s \tag{1}$$

where $G$, $U$, $T$, $S$, $P$, $V$, σ, s represent Gibbs free energy, internal energy, temperature, entropy, pressure, volume, unit surface energy, and surface area respectively, and σs stands for surface energy. At the transition pressure $P$ and constant temperature $T$, Gibbs energy difference is expressed by Eq. (2):

$$\Delta G = \Delta U - T\Delta S + P\Delta V + \Delta(\sigma s) \tag{2}$$

Comparing with bulk materials, $\Delta V$ and $\Delta(\sigma s)$ of nanostructures are the main origin of energy barrier difference. In compression process, $\Delta V$ is negative, but $\Delta(\gamma s)\Delta(\sigma s)$ is positive. They work adversely for the Gibbs free energy change.

### 2.2. Formation of Se nanoribbons with assistance of Sb nanopartiles

The Se plate with purity as 99.99% was fixed in a columned vessel (Φ 6 cm) which was filled with 15 mL deionized water. Then, the irradiation source generated by a 1064 nm Nd:YAG pulsed laser was introduced to ablate the top surface of Se plate with 10 Hz pulse repetition rate, 6 ns pulse duration, and 24 mJ pulse energy density. After 2 min of laser ablation, such formed solution was transferred into another columned vessel in which a Sb plate (99.99% purity) was fixed and then ablated for 10 min with the same laser conditions. The final solution was statically placed at room temperature and then flocculated after a week which meant the formation of Se nanoribbons. After centrifugal separation for 5 min at 8000 rpm, the precipitated Se nanoribbons could be separated from Sb nanoparticles reserved in supernatant. Scheme 1 illustrated the formation process of such nanoribbons.

### 2.3. Characterization of Se nanoribbons

An FEI Sirion 200 FESEM was used to evaluate the morphology of the nanoribbon product. The crystalline structure was investigated on HRTEM (JEM, JEOL-2010). The phase structure was investigated by using XRD with the use of a Philips diffractometer (X'pert Pro) with Cu-$K_\alpha$ radiation ($\lambda$ = 1.5419 Å). Diffused reflection spectroscopy of Se nanoribbons powder was carried out using a Shimadzu UV-2550 spectrometer and the corresponding UV–vis diffuse reflectance spectra were converted to visualized absorption spectra. The energy band gap ($E_g$) is deduced from the absorption data via Eq. (3):

$$\alpha h\nu \quad \propto (h\nu - E_g)^2 \tag{3}$$

Where $h\nu$ is the photon energy and $\alpha$ is the optical absorption coefficient near the fundamental absorption edge.

### 2.4. Raman scattering measurements under high pressure

The Diacell ST type diamond anvil cell (DAC) made of nonmagnetic Cu-Be alloy was utilized to generate high pressure. Diamond anvils were chosen as 200 μm culets, and silicone oil was the pressure-transmitting medium. The rhenium gasket (thickness 40 μm) with a microhole (Φ120 μm) could hold the Se nanoribbons and ruby balls as the sample and the pressure marker respectively. The value of pressure was calibrated by measuring the ruby fluorescence shift at room temperature. The Horiba Jobin Yvon T64000 spectrometer equipped with liquid nitrogen cooled charge-coupled device carried out Raman scattering measurements at room temperature. The measurements were conducted in the form of pseudo backscattering configuration by using 532 nm solid state laser (torus 532, Laser Quantum). The power of laser was below 0.1 mW to avoid sample damage and any heating effect, while the integration time was 150 s. The back-scattered signal was collected in an unpolarized $Y(Z)\bar{Y}$ geometry through 50× objective and 1800 g/mm grating.

### 2.5. Resistance and magnetic susceptibility measurements under high pressure

Here, the screw-pressure-type DAC was also made of nonmagnetic Cu–Be alloy and used to generate pressure. It was fixed inside a multifunctional measurement system (1.8–300 K, JANIS Research Company, Inc.; 0–9 T, Cryomagnetics, Inc.) with helium as the heat convection medium. Diamond anvils of 300-μm culets and T301 stainless-steel gasket covered with a mixture of epoxy and fine cubic boron nitride (cBN) powder were used for high-pressure transport measurements. Se nanoribbons and ruby balls were both put in the sample chamber at the center of the gasket with Daphne 7373 oil as the pressure-transmitting medium. The four-probe method was applied in the resistance measurements of Se nanoribbons. Platinum (Pt) foil with a thickness of 5 μm was used for the electrodes. The high-pressure ac

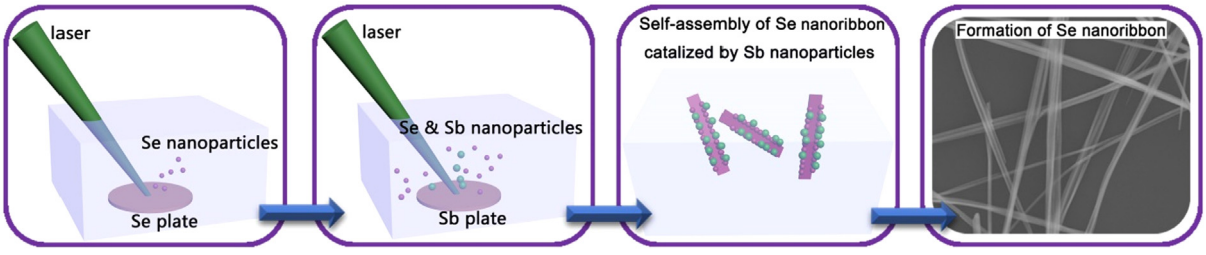


**Scheme 1.** Schematic illustration of Se nanoribbons by laser ablation of Se in water and subsequent catalyzed growth in Sb colloid solution.

magnetic susceptibility was measured by using magnetic inductance technique.

### 2.6. Computational details

First principle calculations were performed to calculate the surface energy of ($\bar{1}20$) plane of selenium. The structure relaxation and total-energy calculation are carried out using the density functional theory within the generalized gradient approximation (GGA), as implemented in the VASP 5.3 package [24]. Electronic exchange and correlation are described by Perdew–Burke–Ernzerhof (PBE) functional [25]. All-electron plane-wave basis sets with the projector augmented wave (PAW) potentials are adopted with 4s24p4 treated as valence electron configuration for Se atom, and the cutoff energy is set to be 300 eV. A dense enough k points sampling is checked with energy tolerance in 1 meV/atom. The surfaces are represented by periodic slab models. A vacuum larger than 10 Å thick is inserted in each model to avoid interaction with imaging free surfaces. The ground state geometries are obtained by minimizing the forces on each atom to be less than 0.01 eV/Å. Surface energy $E_{sur}$ is defined as$E_{sur} = (E_{tot} - N*E_b)/A$, where $E_{tot}$ is energy of the optimized ($\bar{1}20$) slab, $E_b$ is the energy of per atom in bulk selenium, N is the number of atoms in the slab and A is the area of the slab. For the bulk selenium, we obtain the optimized lattice parameters of a = b = 4.48 Å, c = 5.06 Å, which is slightly larger than the experimental value of a = b = 4.36 Å, c = 4.95 Å.

## 3. Results and discussion

### 3.1. Surface and formation of Se nanoribbons

Fig. 1a shows the typical morphology of as-synthesized nanoribbons with the width from 100 nm to 500 nm. The low-resolution SEM image of Fig. S1a in supplementary material shows the large length–diameter ratios of such nanoribbons. The X-ray diffraction (XRD) pattern in Fig. S1b can be indexed to the hexagonal phase of Se (JCPDS card No. 42-1425). Based on Bragg's Law, the crystal lattice parameters were decuced as a = b = 4.370 Å and c = 4.959 Å. Fig. 1b shows the typical bright-field TEM image of Se nanoribbons. The corresponding high-resolution TEM lattice image (Fig. 1d) from the yellow square of a single nanoribbon and selected-area electron diffraction (SAED) pattern (Fig. 1c) clearly demonstrate the single crystalline nature of Se nanoribbons with exposed (1 0 0) and (0 0 1) plane facets [13]. According to the crystal structure of the hexagon-structured Se, the top facets of Se nanoribbons should be ± ($\bar{1}20$) which are simultaneously vertical to (1 0 0) and (0 0 1) facets (Fig. 1e). By theoretical computation, the surface energy of Se nanoribbons was calculated to be 0.069 J/m$^2$, which was larger than that of other one dimensional Se nanostructures (e.g. 0.028 J/m$^2$ of hexagonal Se nanowires) [21,26]. The discussion on the influences of sizes and surface energies on Se nanoribbons will be shown in the following content.

Fig. 2 supported the TEM images of Se nanoribbons at different growth stages. In Fig. 2a, the freshly ablated Se colloidal species were all amorphous clumps without regular shape. After subsequent ablation of Sb plate in above Se colloid solution, the Se clumps mixed with tiny Sb nanoparticles in Fig. 2b. After statically placing for 3 days at room temperature, we could obviously observe flocculation at the bottom of colloidal solution and it would gradually pile up with increasing standing time. In Fig. 2c and d, the flocculation analyzed by TEM technique was proved to be crystalized Se nanoribbons with curly shape and many Sb nanoparticles accumulated on them. 7 days later, in Fig. 2e and f, more Se nanoribbons formed, but no obvious Sb nanoparticles were found. Dark-field transmission electron microscopy image and corresponding energy-dispersive spectroscopy (EDS) mapping analysis of the final Se nanoribbons (Fig. S3 in supplementary material) indicated that the atomic ratio of Sb element was just 0.57%. So, the reserved Sb element in Se nanoribbons could be neglected here. In parallel experiment, Se colloidal solution was statically placed alone at the same conditions with the mixed colloid of Se and Sb (see Fig. S2 in supplementary material). After 34 days, amorphous Se clumps still existed and only a little transformed into nanoribbons. The spontaneous growth of Se clumps in water was much slower than that in mixed colloidal solution. What's more, as the non-contaminating metal catalysts, antimony, bismuth and indium elements usually had low eutectic temperature with semimetals so as to be introduced to accelerate the growth of one dimensional nanostructures [22,23]. We assumed that, Se clumps, with the catalytic assistance of Sb nanoparticles, could quickly orientated grow and crystalized as nanoribbons.

### 3.2. S-M transition of Se nanoribbons

We analyzed the experimental transition pressure of the Se nanoribbons via in situ Raman scattering technique. Fig. 3 presents the Raman spectra from the ambient condition to the highest pressure at 44.8 GPa. Before loading pressure, the Raman peak at 145 cm$^{-1}$ was the $E'$ mode, which was induced by the rotational motions around the axis vertical to the c-axis as the direction of the spiraling of Se atoms

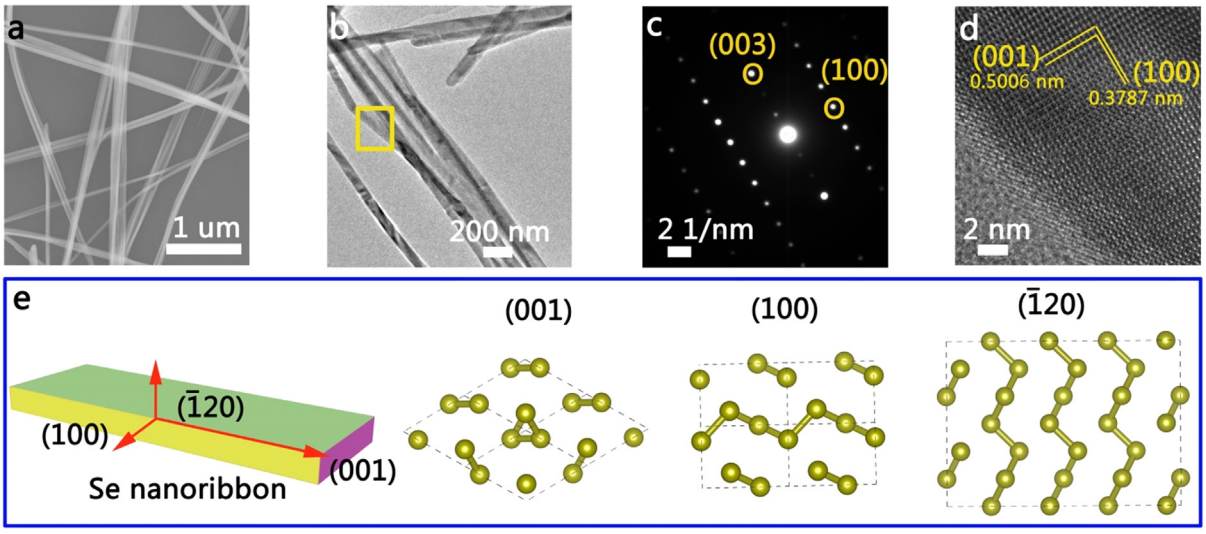


**Fig. 1.** Morphologies and structures of the synthesized hexagonal Se nanoribbons: a. low-resolution SEM image, b. low-resolution TEM image, c. SAED pattern of the yellow part in b, d. HRTEM image corresponding to c, e. schematic structure of the Se nanoribbon and atom distribution of the exposed facets.

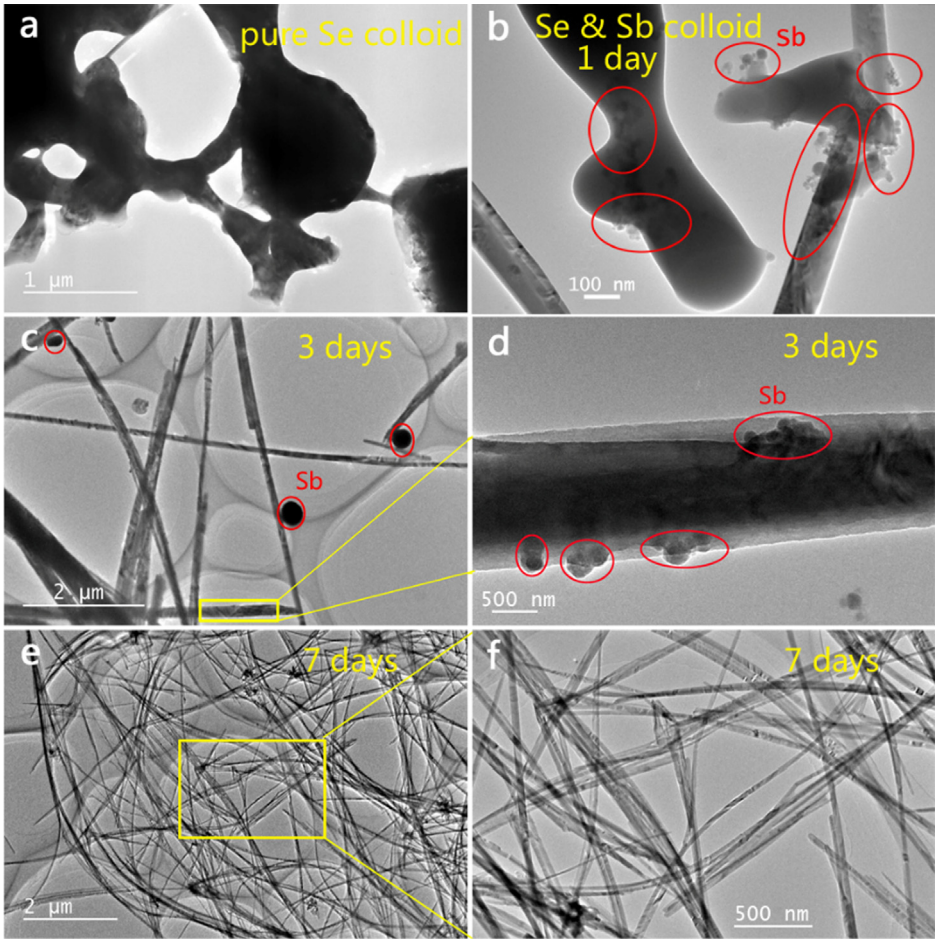


**Fig. 2.** TEM images of Se nanoribbons at different stages: a. Se clumps freshly ablated in water, b. Se clumps mixed with Sb nanoparticles standing for 1 day, c. Se nanoribbons mixed with Sb nanoparticles standing for 3 days, d. magnified image of yellow part in c, e. Se nanoribbons standing for 7 days, f. magnified image of yellow part in e.

[21]. The band centered at 238 $cm^{-1}$ was overlapped by $A_1$ mode and $E''$ mode simultaneously. The former mode was caused by the helical chain-expansion-type lattice vibration, whereas the latter mode was due to asymmetric breathing motions [20]. At increased pressure, $E'$ mode shifted to a high frequency and then disappeared above 11.1 GPa. Upon compression, the peak at 238 $cm^{-1}$ first shifted to a low frequency, indicating the softening of the $A_1$ and $E''$ modes, and then split into two peaks above 1.3 GPa ($A_1$ mode at 211 $cm^{-1}$ and $E''$ mode at 224 $cm^{-1}$). The $A_1$ mode continued to soften with increasing pressure initially, but maintained at around 182 $cm^{-1}$ above 18 GPa. By contrast, the $E''$ mode first shifted to the lowest frequency at 4.6 GPa and then to a high frequency adversely from 6.7 GPa to 44.8 GPa. The softening of the Raman mode indicated that the primary bonding in the Se crystal weakened and the corresponding bond length increased with increasing pressure [27]. The softening of the $A_1$ mode implied a pressure-induced strengthening of the interchain bonds and a

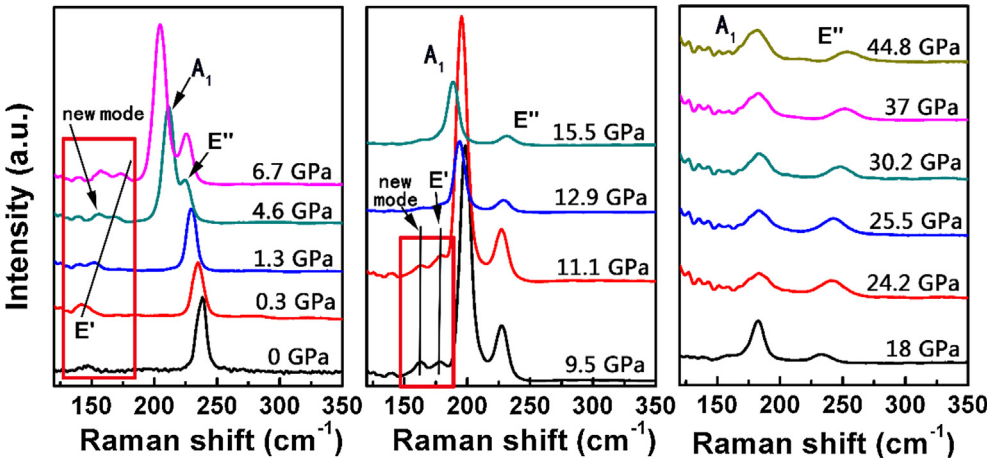


**Fig. 3.** Raman spectra of Se nanoribbons under various pressures.

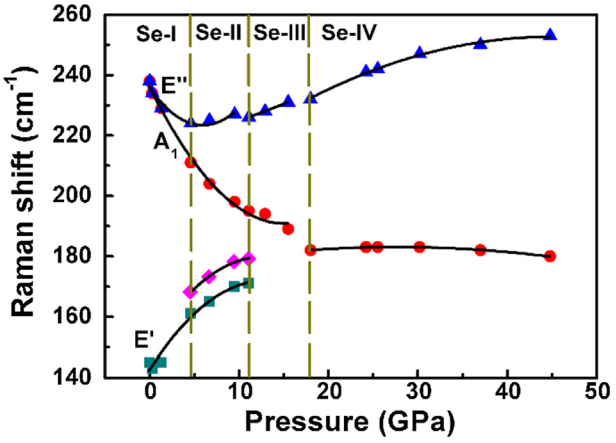


**Fig. 4.** Pressure dependence of Raman shifts of Se nanoribbons. The symbols are experimental data and the solid curves represent the second order polynomial fits.

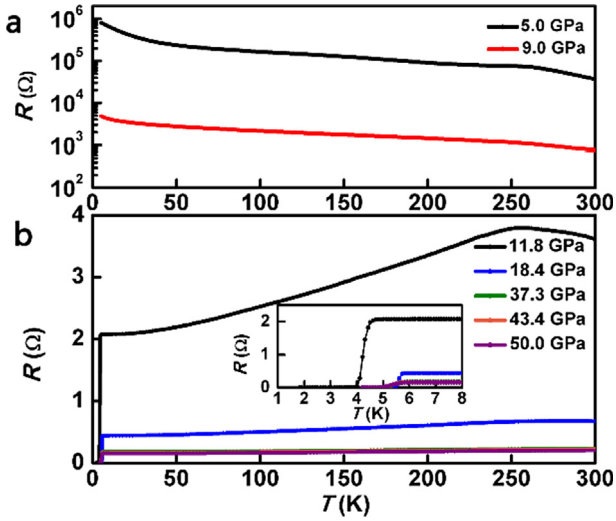


**Fig. 5.** Temperature dependence of resistance of Se nanoribbons under pressures.

weakening of the intrachain bonds. This phenomenon was considered as the beginning of the breakdown of the hexagonal structure [27]. Beginning with 4.6 GPa, a new mode around 170 $cm^{-1}$ emerged, shifted to higher frequency with increasing pressure, and finally disappeared beyond 11.1 GPa. This mode was also observed for Se nanocrystalline upon compression, but its mechanism remains unclear [20]. With the gradual release of pressure to 1 bar, the Raman spectrum reverted to its original form (Fig. S4) in the same manner as that of Se nanocrystalline and Se nanowires.

The Raman shift values of each mode at increasing pressure are labeled in Fig. 4 to enable to the clear observation of the shifting trend of the Raman modes. The symbols indicate experimental data, while the solid curves represent the second order polynomial fits according to Eq. (4):

$$\omega(P) = \omega_0 + c_1 P + c_2 P^2 \quad (4)$$

where $\omega(P)$ and $\omega_0$ represent the Raman shift at pressure and ambient condition respectively, and values of $\omega_0$, $c_1 c_1$ and $c_2$ are all listed in Table S1 in supplementary material.

In Fig. 4, the initial hexagonal structure of Se nanoribbons is collectively labeled as Se-I, while the other structures under a high pressure are denoted as Se-II, Se-III, and Se-IV. In experiments, the $E''$ mode of Se-I diminished to the minimum at 4.6 GPa and then gradually increased with increasing pressure. This sudden change in the shifting trend of the $E''$ mode and the simultaneous appearance of a new peak at around 170 $cm^{-1}$ at 4.6 GPa indicated that the first structure transition occurred from the original hexagonal phase (Se-I) to a new structure (Se-II). This phenomenon was in agreement with the trend of Se nanocrystallines, with the first transition occurring at 5.6 GPa, but the structure information of Se-II was still unknown [20]. Up to 11.1 GPa in Fig. 4, the shifting trend of the $E''$ mode and $A_1$ mode were disrupted, while the $E'$ mode and the new peak both disappeared due to the pressure-induced further distortion of the Se nanoribbon structures. Notably, the disappearance of $E'$ mode is usually followed by the structure transition to metallic monoclinic phase (Se-III) [20,21], indicating that the Se-II structure is unstable. Furthermore, at 11.1 GPa, the $A_1$ mode and $E''$ mode shifted to 195 and 227 $cm^{-1}$ respectively, and both modes located within the range of monoclinic Se [21], also indicating the second transition from Se-II to Se-III. When the pressure was higher than 18.0 GPa, the $E''$ mode remained shifting to high frequencies with increasing pressure, but the rapid softening trend of the $A_1$ mode was interrupted. The $A_1$ mode sharply declined from 15.5 GPa to 18.0 GPa, indicating further distortion in the helical chain structure so as to the entire disjoint of the chainlike microstructures of the Se nanoribbons [20]. This indicated the structure transition from the Se-III phase to the Se-IV phase.

The temperature dependence of resistance for Se nanoribbons under various pressures was measured (Fig. 5) to understand the S-M transition of Se nanoribbons. The temperature ranged from 300 K to 1.8 K. At 5.0 and 9.0 GPa (Fig. 5a), both curves show typical semiconductor features with resistance magnitude of $10^5$ and 103 O, respectively. In Fig. 5b, at 11.8 GPa, the resistance decreased to several ohms. The monotonically increasing and nearly linear relationship with temperature confirmed the metallic nature of the Se nanoribbons. According to the Raman measurement, a monoclinic Se-III phase formed at 11.1 GPa, so an S-M transition occurred. When the temperature decreased to around 5 K, the resistance immediately decreased to approximately 0 O, indicating the superconducting feature of the Se nanoribbons. This feature is the same as that of bulk Se-III; the Se nanoribbons are superconductive at cryogenic conditions and conductive at room temperature [5,9,28]. From 11.8 GPa to 18.4 GPa, the resistance further decreased indicating that the structure became increasingly distorted. The resistance deviation also confirmed the transition from Se-III to Se-IV as same as the results of Raman measurement. The antimagnetic abilities of the Se nanoribbons were also observed at 18.4 GPa (Fig. S5), and the superconductive transition temperature ($T_c$) nearly disappeared at the magnetic field of approximately 2 T. In Fig. 5, the $T_c$ of Se nanoribbons at 11.8 GPa was 4.5 K lower than that of bulk Se (5.6 K) [11], possibly because the thickness of the Se nanoribbons were shorter than the London penetration depth and the coherence length of bulk Se [29].

The Grüneisen parameter γ is usually used to signify the anharmonic effect of phonon vibration. Larger γ indicates more intensive anharmonic vibration so as to longer distance of the corresponding bonded atoms for some Raman mode [30]. Fig. 6 shows the dependence to pressure of the Grüneisen parameters according to Eq. (5). The Grüneisen parameter of $E'$ mode decreased with increasing pressure and kept a positive value under 11.1 GPa. For$E''$ $E''$ mode, the parameter was negative below 4.6 GPa and then turned to positive above 6.7 GPa, while for $A_1A_1$ mode, it was always negative within the experimental pressure range. The rising trend of Grüneisen parameter of $A_1$ mode upon compression indicated enhancing anharmonic effect for interchain bonded atoms followed by final breakdown of interchain bonds. Commonly, strain aroses when a crystal is compressed under pressure, and the strain can modify the crystal phonons, especially, the tensile strain will lead to softening of Raman modes, while the compressive strain can result in the opposite shifting trend of modes [31]. For Se nanoribbons, the continuous softening of $A_1$ mode suggested that the interchain bonds always suffered from a tensile strain which could

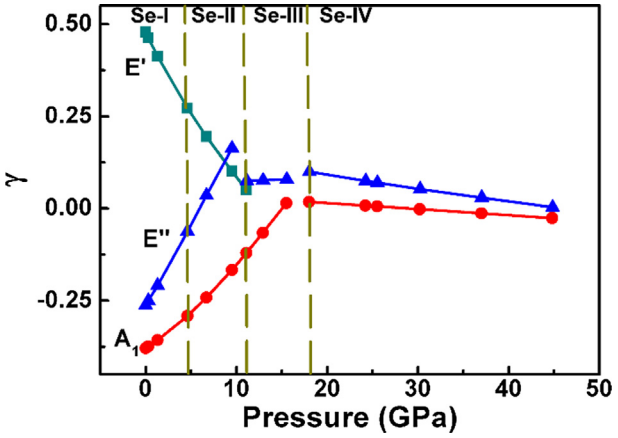


**Fig. 6.** The mode Grüneisen parameter γ of Se nanoribbons.

shear the bonds between spiral chains. The changing trend of γ for $A_1$ mode was consistent with the situation observed in Raman spectra [21].

$$\gamma = -(\frac{\partial \ln \omega}{\partial \ln V}) = \frac{B}{\omega}\frac{d\omega}{dP} \quad (5)$$

The Grüneisen parameter γ is defined as the Eq. (5) in which $\omega\omega$, $V$, $P$ are the frequency of the vibrational mode, the volume and the pressure, and $B$ is the bulk modulus (14.9 GPa for bulk Se).

The above results confirmed that the S-M transition of the Se nanoribbons occurred at 11.1 GPa which matched well with the theoretically predicated value of 11.16 GPa. Notably, our experiment was conducted at room temperature, so the relatively low S-M transition pressure was not attributed to the decreasing of temperature. For the Se nanoribbons, the ± ($\bar{1}$20) planes were the major exposed facets, and the surface energy was calculated as 0.069 J/m$^2$, and the surface energy contribution from side facets was omitted. Pressure-induced shape changes convert nanocrystals with low indexes and low-energy surfaces into deformed nanocrystallines with high indexes and energy surfaces [16]. In phase transition, the surface energies of the Se nanoribbons increased, resulting in increased energy barrier. Meanwhile, shape-dependent compressibility of 1-D nanostructures relates with the crystal structure feature and the growth direction simultaneously [19]. It is easy to find that 1-D nanostructures usually have large compressibility during structural transition so as to decrease the energy barrier for low transition pressures [12,19]. For the solid–solid phase transition in semiconductors, the volumetric contraction between the two phases around the transition pressure was possibly dependent on the energy band gap (Eq. (6)) [21,32]. The absorbance spectrum of the Se nanoribbons and their corresponding energy band gaps are shown in Fig. S6. According to the intercept of a tangent line crossing the horizontal axis, the value of $E_gE_g$ was estimated as 1.75 eV which was higher than that of the bulk as 1.6 eV [1,33]. In view of Eq. (6) suggested by Jamieson [21], the volumetric compression ratio of the Se nanoribbons to the bulk was 3.3, indicating that the densification of nanoribbons under pressure was greater than that of bulk Se. Although temperature can enhance the energy barrier according to Bandyopadhyay's theory [9], such large volumetric contraction can lead to large reductions in energy barriers and may thus offset the energy enhancement induced by surface energy change and temperature, resulting in a lower transition pressure close to the theory transition pressure point.

$$P_T \Delta V = E_g/2 \quad (6)$$

where $\Delta V$ represents the volumetric difference between the two structures around the transition pressure $P_T$. $E_g$ is the energy band gap at ambient pressure.

## 4. Conclusions

We first reported the S–M transition pressure of selenium nanoribbons at 11.1 GPa, which was extremely close to the predicted 11.16 GPa of hexagonal Se. A series of phase transition from Se-I to Se-IV were observed by in-situ Raman spectra. The first phase transition from Se-I to Se-II occurred at 4.6 GPa. The monoclinic Se-III and Se-IV phases emerged at 11.1 and 18 GPa, respectively, and both phases were metallic at room temperature and superconductive at cryogenic temperature. All transition pressures for the Se nanoribbons were lower than the corresponding values of bulk Se. The volumetric contraction offsetting surface energy change of Se nanoribbons during phase transition was thought to be the main cause of the low transition pressures.

## Acknowledgement

This work was financial supported by the National Basic Research Program of China (No. 2014CB931704), the National Natural Science Foundation of China (NSFC No. 51571186, 11504375, 11604320, 11674321) and the Anhui Provincial Natural Science Foundation (1508085QA21).

## Appendix A. Supplementary material

Supplementary data to this article can be found online at https://doi.org/10.1016/j.apsusc.2018.12.183.

## References

[1] R.A. Zingaro, W.C. Cooper, Selenium, Van Nostrand-Reinhold, New York, 1974.
[2] L.I. Berger, Semiconductor Materials, CRC Press, Boca Raton, 1997.
[3] Y. Akahama, M. Kobayashi, H. Kawamura, Structural studies of pressure-induced phase transitions in selenium up to 150 GPa, Phys. Rev. B 47 (1993) 20–26.
[4] C. Hejny, M.I. McMahon, Complex crystal structures of Te-II and Se-III at high pressure, Phys. Rev. B 70 (2004) 184109.
[5] Y. Akahama, M. Kobayashi, H. Kawamura, Pressure-induced superconductivity and phase transition in selenium and tellurium, Solid State Commun. 84 (1992) 803–806.
[6] G. Parthasarathy, W.B. Holzapfel, Structural phase transitions and equations of state for selenium under pressure, Phys. Rev. B 38 (1988) 10105.
[7] J. Wittig, Stability of the metallic state of selenium under pressure, J. Chem. Phys. 58 (1973) 2220–2222.
[8] E. Gregoryanz, V.V. Struzhkin, R.J. Hemley, M.I. Eremets, H.K. Mao, Y.A. Timofeev, Superconductivity in the chalcogens up to multimegabar pressures, Phys. Rev. B 65 (2002) 064504.
[9] D. Singh, A.K. Bandyopadhyay, M. Rajagopalan, P.C. Sahu, M. Yousuf, K.G. Rajan, Electronic band structure calculation and structural stability of high pressure phases of selenium, Solid State Commun. 109 (1999) 339–344.
[10] K.F. Yang, Q.L. Cui, Y.Y. Hou, B.B. Liu, Q. Zhou, J.Z. Hu, H.K. Mao, G.T. Zou, Pressure-induced crystallization and phase transformation of amorphous selenium: Raman spectroscopy and x-ray diffraction studies, J. Phys.: Condens. Matter. 19 (2007) 425220.
[11] Y. Akahama, M. Kobayashi, H. Kawamura, Pressure-induced metallization and structural transition of α-monoclinic and amorphous Se, Phys. Rev. B 56 (1997) 5027–5031.
[12] Z.P. Li, B.B. Liu, S.D. Yu, J.H. Wang, Q.J. Li, B. Zou, T. Cui, The Study of Structural Transition of ZnS Nanorods under High Pressure, J. Phys. Chem. C 115 (2011) 357–361.
[13] Z.W. Wang, L.L. Daemen, Y.S. Zhao, C.S. Zha, R.T. Downs, X.D. Wang, Z.L. Wang, R.J. Hemley, Morphology-tuned wurtzite-type ZnS nanobelts, Nature Mater. 4 (2005) 922–927.
[14] S.H. Tolbert, A.P. Alivisatos, Size dependence of a first order solid-solid phase transition: The Wurtzite to rock salt transformation in CdSe nanocrystals, Science 265 (1994) 373–376.
[15] S.H. Tolbert, A.P. Alivisatos, The wurtzite to rock salt structural transformation in CdSe nanocrystals under high pressure, J. Chem. Phys. 102 (1995) 4642–4656.
[16] S.H. Tolbert, A.B. Herhold, L.E. Brus, A.P. Alivisatos, Pressure-Induced Structural Transformations in Si Nanocrystals: Surface and Shape Effects, Phys. Rev. Lett. 76 (1996) 4384–4387.
[17] J.Z. Jiang, J.S. Olsen, L. Gerward, S. Morup, Enhanced bulk modulus and reduced transition pressure in γ-$Fe_2O_3$ nanocrystals, Europhys. Lett. 44 (1998) 620–626.
[18] J.S. Olsen, L. Gerward, J.Z. Jiang, On the rutile/α-$PbO_2$-type phase boundary of $TiO_2$, J. Phys. Chem. Solids 60 (1999) 229–233.
[19] Q.J. Li, B.Y. Cheng, X. Yang, R. Liu, B. Liu, J. Liu, Z.Q. Chen, B. Zou, T. Cui, B.B. Liu, Morphology-tuned phase transitions of anatase $TiO_2$ nanowires under high pressure, J. Phys. Chem. C 117 (2013) 8516–8521.
[20] H.Z. Liu, C.Q. Jin, Y.H. Zhao, Pressure induced structural transitions in

nanocrystalline grained selenium, Physica B 315 (2002) 210–214.
[21] R.C. Dai, L.B. Luo, Z.M. Zhang, Z.J. Ding, Raman studies of selenium nanowires under high pressure, Mater. Res. Bull 46 (2011) 350–354.
[22] X.H. Sun, G. Calebotta, B. Yu, G. Selvaduray, M. Meyyappan, Synthesis of germanium nanowires on insulator catalyzed by indium or antimony, J. Vac. Sci. Technol. B 25 (2007) 415–420.
[23] C.Y. Yan, P.S. Lee, Bismuth-catalyzed growth of germanium nanowires in vapor phase, J. Phys. Chem. C 113 (2009) 2208–2211.
[24] G. Kresse, J. Furthmüller, Efficient iterative schemes for ab initio total-energy calculations using a plane-wave basis set, Phys. Rev. B 54 (1996) 11169–11186.
[25] J.P. Perdew, K. Burke, M. Ernzerhof, Generalized gradient approximation made simple, Phys. Rev. Lett. 77 (1996) 3865–3868.
[26] M.U. Kahaly, P. Ghosh, S. Narasimhan, U.V. Waghmare, Size dependence of structural, electronic, elastic, and optical properties of selenium nanowires: A first-principles study, J. Chem. Phys. 128 (2008) 044718.
[27] K. Nagata, T. Ishikawa, Y. Miyamoto, Raman Spectra of Rhombohedral and α-Monoclinic Selenium under High Hydrostatic Pressure, Jpn. J. Appl. Phys. 22 (1983) 1129–1132.
[28] O. Degtyareva, E. Gregoryanz, M. Somayazulu, H.K. Mao, R.J. Hemley, Crystal structure of the superconducting phases of S and Se, Phys. Rev. B 71 (2005) 214104.
[29] W.H. Li, C.C. Yang, F.C. Tsao, K.C. Lee, Quantum size effects on the superconducting parameters of zero-dimensional Pb nanoparticles, Phys. Rev. B 68 (2003) 184507.
[30] A.F. Goncharov, V.V. Struzhkin, E. Gregoryanz, J.Z. Hu, R.J. Hemley, H.K. Mao, Raman spectrum and lattice parameters of $MgB_2$ as a function of pressure, Phys. Rev. B 64 (2001) 100509.
[31] J. Zabel, R.R. Nair, A. Ott, T. Georgiou, A.K. Geim, K.S. Novoselov, C. Casiraghi, Raman spectroscopy of graphene and bilayer under biaxial strain: Bubbles and balloons, Nano Letters 12 (2012) 617–621.
[32] J.C. Jamieson, Crystal structures at high pressures of metallic modifications of compounds of indium gallium, and aluminum, Science 139 (1963) 845–847.
[33] B. Gates, B. Mayers, B. Cattle, Y. Xia, Synthesis and characterization of uniform nanowires of trigonal selenium, Adv. Funct. Mater. 12 (2002) 219–227.